

Two Dimensional Vortex Shedding from a Rotating Cluster of Cylinders

B. B. Ndebele^{1†} and I. M. A. Gledhill²

¹ CSIR, Department of Defence, and Security, Pretoria, Gauteng, 0001, South Africa

² Department of Mechanical, Industrial, and Aeronautical Engineering, University of the Witwatersrand, Johannesburg, 2000, South Africa

†Corresponding Author Email: bndebele@csir.co.za

ABSTRACT

The dynamics of two-dimensional vortex shedding from a rotating cluster of three cylinders was investigated using Computational Fluid Dynamics (CFD) and Dynamic Mode Decomposition (DMD). The cluster was formed from three circles with equal diameters in mutual contact and allowed to rotate about an axis passing through the cluster centroid. While immersed in an incompressible fluid with Reynolds number of 100, the cluster was allowed to rotate at non-dimensionalised rotation rates (Ω) between 0 and 1. The rotation rates were non-dimensionalised using the free-stream velocity and the cluster characteristic diameter, the latter being equal to the diameter of the circle circumscribing the cluster. CFD simulations were performed using StarCCM+. Dynamic Mode Decomposition based on the two-dimensional vorticity field was used to decompose the field into its fundamental mode-shapes. It was then possible to relate the mode-shapes to lift and drag. Transverse and longitudinal mode-shapes corresponded to lift and drag, respectively. Lift–drag polars showed a more complex pattern dependent on Ω in which the flow fields could be classified into three regimes: Ω less than 0.3, greater than 0.5, and between 0.3 and 0.5. In general, the polars formed open curves in contrast to those of static cylinders, which were closed. However, some cases, such as $\Omega = 0.01, 0.22,$ and $0.28,$ formed closed curves. Whether a lift-drag polar was closed or open was deduced to be determined by the ratio of Strouhal numbers calculated using lift and drag time series, with closed curves forming when the ratio is an integer.

Article History

Received January 31, 2023

Revised July 13, 2023

Accepted July 17, 2023

Available online September 3, 2023

Keywords:

Vortex shedding

Rotating cylinders

Computational Fluid Dynamics

Dynamic Mode Decomposition

1. INTRODUCTION

Vortex shedding is widespread in nature and in engineering, and its analysis is indispensable in the study and application of fluid mechanics. For example, vortices are shed around tall buildings, sub-sea cables, and power-lines and may cause these structures to oscillate. In extreme cases, the resulting oscillations can be disastrous if the frequency of oscillation matches one of the structure's modal frequencies. On a larger scale, vortices are shed around islands in the sea (Inoue et al., 2013). In the examples cited above, the objects from which vortices are shed each have contrasting shapes from each other: compare the irregular shape of an island with that of a skyscraper. However, considerable insight, applicable to many configurations, has been obtained from the consideration of the shedding of vortices from cylinders.

Vortex shedding from cylinders in different configurations is a subject of study that has been addressed by many authors. Matharu et al. (2021) considered the flow around a cylinder oscillating transversely to the free-stream, an extension to the seminal paper of Williamson and Roshko (1988). The oscillations result in a wake whose topology depends on the ratio of the period (τ_c) and amplitude (A_c) of the cylinder oscillation in addition to the free-stream Reynolds number (Re). It is found that the wake differs from the general Von Kármán vortex street by the existence of a break in symmetry as a function of τ_c and A_c . Matharu et al. (2021) found that at $Re = 100$, vortex shedding can occur via a pair of counter-rotating vortices or a combination of a single vortex and a pair of counter-rotating vortices. Consider vortices on one side of the centre line; if a single shed vortex as is labelled as S and a pair of shed vortices as P, then the first and second modes

NOMENCLATURE			
A_c	amplitude of oscillation	T	oscillation period
b_i	initial mode shape amplitude	U_∞	free stream velocity
C	Courant number	\mathbf{v}	fluid velocity
C_D	drag coefficient	x	arbitrary vector field
C_L	lift coefficient	α	angle step
D	cylinder diameter	Δ_{\min}	minimum cell size
E	Energy	Δt	time step
f	Frequency	Δx	grid size
\mathbf{f}_b	resultant body force	ε	relative error
GCI	Grid Convergence Index	ζ	vorticity
n	number of time steps	ρ	Density
p	numerical scheme order	σ	stress tensor
Q_i	measured quantity in CFD	τ_c	wake period of oscillation
r	grid or temporal discretisation ratio	$[\varphi_i]$	set of mode shapes
Re	Reynolds number	$[\omega_i]$	set of eigenvalues
S_i	stagnation points	ω	rotation rate
St	Strouhal number	Ω	non-dimensionalised rotation rate

by Matharu et al. (2021) are labelled 2S and P+S, i.e., S vortices on either side of the centre line and P and S vortices on either side of the centre line respectively. The modes of vortex shedding can be more complicated, as illustrated by Williamson and Roshko where it was shown that shedding in 2P and 2P+2S amongst other modes is possible.

Mittal and Kumar (2003) studied the flow past a rotating cylinder and the resulting wake. Rotating cylinders find application in flow-control and drag reduction (Schulmeister et al., 2017). With rotation, the cylinder experiences the Magnus effect in addition to lift and drag, which leads to the possibility of using rotating cylinders as lift producing devices. The rotating cylinder problem can be characterized by two parameters, Re and the non-dimensionalised rotation rate (Ω) defined to be $\Omega = \omega D/2U_\infty$ where ω is the rotation rate, D is the reference diameter, and U_∞ the free stream velocity. Mittal and Kumar (2003) investigated this flow for $Re = 200$ and $0 \leq \Omega \leq 5$. When $0 \leq \Omega \leq 1.9$ a Von Kármán street was observed in the wake with deviations from the centre line for $\Omega > 0$. Within this range, increasing rotation rates corresponding to a thinning wake and a reduction in Strouhal number ($St = fD/U_\infty$, where f is the vortex shedding frequency). For $1.9 \leq \Omega \leq 4.34$, the flow is stable but loses stability when $\Omega \sim 4.35$ which it regains when $\Omega \geq 4.8$. An unstable flow tends towards different states, dependent on whether the rotating cylinder is impulsively started or smoothly accelerated to its final steady rotation rate, implying dependence on flow history.

Other scenarios different from the two mentioned above were investigated by Chen et al. (2020), Sumner et al. (2000), and Carmo et al. (2008); the former considered a cluster of three cylinders arranged with their centres at the vertices of an equilateral triangle, while the latter two used a cluster of two cylinders. In each case, the parameter space is composed of Re and the spacing between cylinders, L (non-dimensionalised by the cylinder diameter, L/D). Obviously, the implication of mutual cylinder proximity and contiguity is the interaction of

vortices and shear-layers of one cylinder with those of another. In a review, Zdravkovich (1977) classified the flow between around a pair of cylinders into three categories: extended flow, reattachment, and co-shedding. Extended flow occurs when the free shear layer from the leading cylinder over-shoots the adjacent cylinder, leaving the region between the cylinders stagnant; reattachment occurs when the free shear layer later reattaches onto the adjacent cylinder; and co-shedding occurs when the spacing between cylinders is sufficiently large for both cylinders to shed vortices. The category of flow attained is determined by L/D and Re . Chen et al. (2020) found that when L/D is between 1.0 and 1.4 and $Re = 150$, the cluster of three cylinders behaves as if it were a single bluff body. With one leading cylinder (and two rear cylinders), the shear layer that forms on the upstream cylinder reattaches on the two downstream cylinders. Thereafter, a typical Von Kármán street forms in the wake shed alternately from the two downstream cylinders. Although not investigated by Chen et al. (2020), a mirror reflection of this arrangement should result in a shear layer separating from the now two upstream cylinders without interacting with the downstream cylinder. As L/D is increased beyond 1.4, a greater spacing between cylinders shifts the point of shear layer reattachment until eventually a vortex street develops from an individual cylinder. Another similar investigation was that by Wang et al. (1996) who investigated vortex shedding about a freely rotating triangular cylinder. Their results show that vortex shedding mode and the behaviour of the cylinder depends on Re . They show that the triangular cylinder can remain at rest, perform rotational oscillations, autorotation, or random rotations. The last rotation mode is the most intriguing; Wang et al. (1996) describe it as intermittent rotations at $Re = 130$. Slightly similar investigations were conducted by Bai et al. (2021) where they consider a magnus rotor. They find that the wake behind the spinning rotor is strictly three dimensional. Consider cylinders of equal diameter in configurations shown in Fig. 1 with a fluid flowing from left to right: each configuration is considered separately. Shown in Fig. 1a,

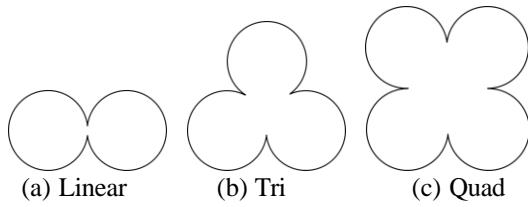


Fig. 1 A cluster of cylinders arranged on the vertices of regular shapes. In (a), the cylinder centres are at opposite ends of a straight line; in (b), the cylinders are at the vertices of an equilateral triangle; and in (c), the cylinder centres are at the vertices of a square

b, and c are two, three, and four tangential cylinders. The cylinder arrangements are similar to those considered by [Chen et al. \(2020\)](#), [Zdravkovich \(1977\)](#), [Sumner et al. \(2000\)](#), and [Carmo et al. \(2008\)](#). The cluster of cylinders is then allowed to rotate about its centroid, making this case similar to that considered by [Mittal and Kumar \(2003\)](#). Finally, as the cluster rotates, the surface area normal to the free-stream increases and decreases as a function of rotation rate; without stretching the analogies too far, but this may be considered to be similar to the cylinder oscillation case studied by [Matharu et al. \(2021\)](#).

This paper presents the investigation of the influence of rotation on vortex shedding around the three cylinder arrangement at $Re = 100$ and $0 \leq \Omega \leq 1.0$. In this investigation, the cylinder cluster is forced to rotate at some fixed rate unlike in [Wang et al. \(1996\)](#) where the triangular cylinder is free to rotate, and [Matharu et al. \(2021\)](#) where the cylinder is oscillated in the vertical plane. As such, this work serves as an extension of their investigations. Dynamic Mode Decomposition (DMD) was then used to extract mode-shapes of the vortex street, after which the modes are shown to be related to lift and drag variations.

The methodology followed in this study is presented in Section 2., the results and discussion are presented in Section 3., and the conclusions in Section 4.

2. METHODOLOGY

The interaction of the fluid with the rotating cylinder cluster is investigated using Computation Fluid Dynamics (CFD), which results were analysed using dynamic mode decomposition (DMD) ([Schmid, 2010](#); [Taira et al., 2017](#)) to extract the fluid flow modes. Since this is an exploration of flow phenomena rather than computational fluid dynamics aspects, it was considered reasonable to use existing software that is well-validated in the incompressible range. As such, CFD simulations were performed using the commercial solver StarCCM+ and the DMD code was written in Python 2.7.16. The bulk of the CFD simulations were run on the Centre for High Performance Computing cluster (CHPC, South Africa) while DMD analyses and some CFD exploration studies were run on a local PC with 32 GB of RAM, an Intel Core i7-4810MQ processor clocked at 2.80 GHz, and running Fedora 30.

2.1 Computational Fluid Dynamics

A two-dimensional laminar implicit unsteady flow solver was set up to solve the incompressible Navier-Stokes equations (Eq. 1). \mathbf{U} , \mathbf{Q} , and \mathbf{R} are as shown in Eq. (2) where $\boldsymbol{\sigma}$ is the stress tensor, \mathbf{f}_b the resultant body force, \mathbf{v} the fluid velocity, ρ is fluid density, and E is energy content.

$$\frac{\partial \mathbf{U}}{\partial t} + \nabla \cdot \mathbf{Q} = \mathbf{R} \quad (1)$$

$$\mathbf{U} = \begin{pmatrix} \rho \\ \rho \mathbf{v} \\ \rho E \end{pmatrix}, \mathbf{Q} = \begin{pmatrix} \rho \mathbf{v} \\ \rho \mathbf{v} \mathbf{v} \\ \rho E \mathbf{v} \end{pmatrix}, \mathbf{R} = \begin{pmatrix} 0 \\ \Delta \cdot \boldsymbol{\sigma} + \mathbf{f}_b \\ \mathbf{f}_b \cdot \mathbf{v} + \nabla \cdot (\mathbf{v} \cdot \boldsymbol{\sigma}) \end{pmatrix} \quad (2)$$

Cylinder cluster rotation was implemented by using the overset meshing method where the rotating cluster is placed in a foreground mesh which in turn is embedded onto a background mesh. The cell dimensions at the interface of the two meshes were similar, and inspection of the solution did not show any significant distortion of the flow phenomena. The boundary conditions are composed of two symmetry planes sufficiently displaced from the rotating cluster, a fluid inlet, and an outlet. A no-slip boundary condition was applied on all walls (including the rotating cylinder). A thin layer of prism cells was used to mesh the region immediately next to the rotating cluster. Figure 2 shows the dimensions of the domain on which the CFD was performed. In this instance, the characteristic diameter D was chosen to be the diameter of the circle that circumscribes the cluster of cylinders. The overset meshing method was used, in which the cylinder cluster is meshed in a smaller domain overlaid onto a background mesh. A rotation is then imposed on the overset mesh to simulate cylinder cluster rotation. Solution information is shared between the overset and the background mesh at the intersection of the overset mesh boundary with the background mesh.

The fluid was air with a constant density of $1.18 \text{ kg}\cdot\text{m}^{-3}$ and a viscosity of $1.86 \times 10^{-5} \text{ Pa}\cdot\text{s}$. The coupled flow solver was chosen with the Courant number ($C = U_\infty \Delta t / \Delta x$, where Δt is the time-step and Δx the minimum mesh size) set to a constant value of 50. The time step was chosen according to $\Delta t = a/\omega$ where a is the incremental rotation angle; a was chosen to be 1° .

Convergence was determined by monitoring the drag coefficient C_D on the cylinder assembly. If $|C_{D,\text{max}} - C_{D,\text{min}}| < 0.05$ over ten inner iterations, then the solution is judged to have converged for that time-step. Further, the maximum number of inner iterations was limited to 100 and x-, y- momentum values were required to decrease by at least three orders of magnitude. With these settings, each time-step was completed within an average of forty iterations.

A typical mesh on which the CFD was conducted is shown in Fig. 2. The mesh was composed of polyhedral cells and an inflation layer made up of 25 prism layers in the neighbourhood of the cylinder walls. The inflation layer total thickness was set to 1.55 mm and the growth rate between layers set to 1.05 and following the geometric progression series. The overset surface mesh was set to a uniform 5 mm and the growth rate from the walls to the overset set to 1.1. The background mesh definition was

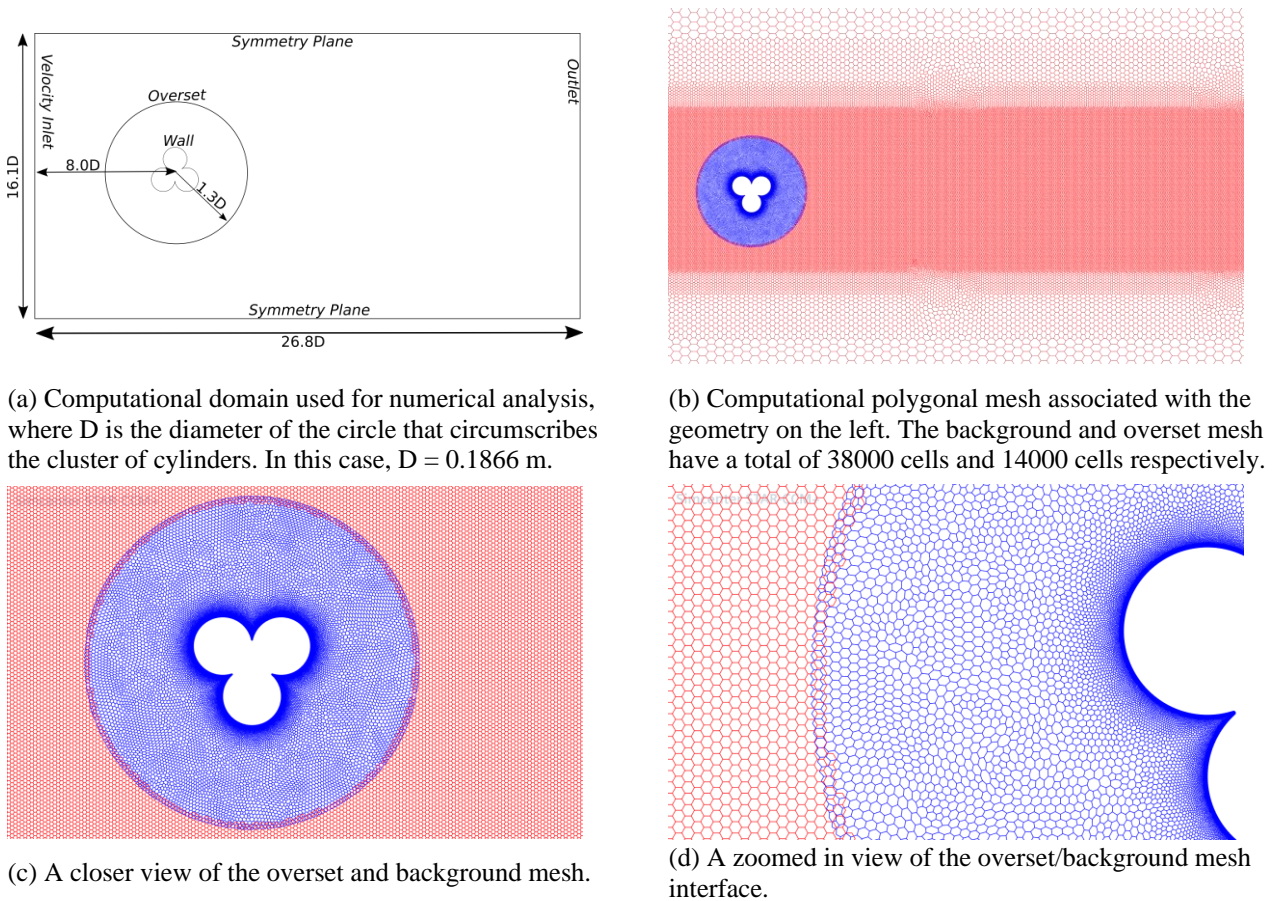


Fig. 2 A sketch of the computational domain used and the corresponding mesh

Table 1 Mesh independence analysis. Drag $\overline{C_D}$ is time averaged. The minimum cell size, Δ_{min} , was measured in the wake excluding the prism layer cells. Mesh variations were achieved by changing the reference length only, since all other mesh parameters were given relative to this value

Grid	#Cells	Δ_{min}	$\overline{C_D}$	St	GCI_D	GCI_{st}
0	560943	0.00625	9.9087	0.2000	0.15%	2.0%
1	227783	0.0125	9.9235	0.2040	1.25%	2.2%
2	103888	0.025	10.048	0.1995	-	-

Table 2 Time independence analysis for the static cases. Drag $\overline{C_D}$ is time averaged over a complete period of oscillation

Case	Δt	$\overline{C_D}$	St	$ \varepsilon_D $	$ \varepsilon_{St} $
0	1.25	10.0197	0.1988	0.5%	1.3%
1	2.50	10.0490	0.2014	1.1%	1.9%
2	3.75	9.9369	0.2052	-	-

simpler with the boundaries set to 50 mm and the region around the cylinder cluster and its wake set to 5 mm. Notice that with these settings, the interface between the overset mesh and the background mesh was guaranteed to have equal cell sizes, this being a strict requirement for a stable simulation.

2.2 Mesh and Time Independence Study

A mesh and time independence study was conducted, and a numerical error estimate determined using Roache's (1994) error estimation method. Using Richardson's extrapolation (Phillips & Roy, 2014), Roache defined a new error estimation term called the Grid Convergence

Index (GCI) (Eq. 3). An expression for GCI is shown in Eq. 3 where r is the ratio between the representative grid size of the coarse and fine mesh ($r > 1$); p is the order of the numerical scheme used (second order, in this paper); and $|\varepsilon|$ is the relative error of quantity of interest between two grids – the fine and coarse grid.

In this paper the coefficient of drag (C_D) and Strouhal number (St) were monitored at different mesh refinement levels and timesteps. Their time-averaged values and convergence indices are shown in Tables 1 and 2. Both tables correspond to a non-rotating cylinder cluster in the right configuration. The GCI represents the discretisation error due to using the corresponding grid. The grid

Table 3 Time independence analysis for the rotating cases. The $\omega = 0.01 \text{ rad.s}^{-1}$ case was used. Drag $\overline{C_D}$ and lift coefficients $\overline{C_L}$ are time averaged over their complete periods of oscillation

Case	$\alpha (\Delta t = \alpha/\omega)$	$\overline{C_D}$	$\overline{C_L}$	St_{major}	St_{minor}	$ \varepsilon_D $	$ \varepsilon_L $	$ \varepsilon_{\text{st, major}} $	$ \varepsilon_{\text{st, minor}} $
0	0.01745	9.4341	-1.7799	0.1056	0.1861	-	-	-	-
1	0.00873	9.4750	-1.7824	0.1068	0.1868	0.5%	0.2%	1.0%	0.4%

Table 4 A comparison of Strouhal numbers (St_S) calculated using StarCCM+ with Roshko's (St_R) results

Re	St_R	St_S	%(Error)
75	0.152	0.155	2%
100	0.167	0.177	6%
125	0.176	0.187	6%

described in the section above is represented by grid-0 in Table 1 and the associated error estimates for using the grid are shown therein. The influence of timestep is shown in Table 2.

$$GCI = \frac{3|\varepsilon|}{r^{p-1}} \text{ where } p = 2 \tag{3}$$

$$\varepsilon = \frac{Q_{\text{fine}} - Q_{\text{coarse}}}{Q_{\text{fine}}} \times 100\% \tag{4}$$

Similarly, Table 3 shows the timestep independence analysis for the rotating cases.

The timestep was calculated as $\Delta t = \alpha/\omega$ with α the incremental rotation angle therefore, analysis was conducted by halving α . In this instance the timestep corresponding to case-0 was used as the relative error between case-0 and case-1 was considered sufficiently small.

2.3 Model Validation

Roshko provided Strouhal numbers of cylinders for Reynolds numbers between 50 and 1400 for cylinders with different diameters. Table 4 shows a comparison between Roshko's findings (Roshko, 1954) and StarCCM+ simulation results. Eq. 5 is the empirical relationship between Reynolds number and Strouhal number derived from Roshko's experimental data. The StarCCM+ results correspond to a cylinder that circumscribes the cylinder cluster that is investigated in this paper and uses an equal time step and similar grid. From the results, it can be seen that StarCCM+ results are consistent with Roshko's findings. The differences were considered sufficiently small to be confident in further simulation results were the cluster of cylinders was considered.

$$St = 0.212 \left(1 - \frac{21.2}{Re} \right) \tag{5}$$

2.4 Dynamic Mode Decomposition (DMD)

Dynamic Mode Decomposition is a data-driven technique which can be used to create reduced order models of linear and non-linear systems (Taira et al., 2020). Consider, for example, the shedding of vortices behind a cylinder; using DMD, the vortex street can be decomposed into several mode-shapes which each represent the dominant structures in the vortex street.

Moreover, the extracted modes can be used to predict the evolution of the flow-field in time and space which in turn allows for predictive control systems to be designed if required.

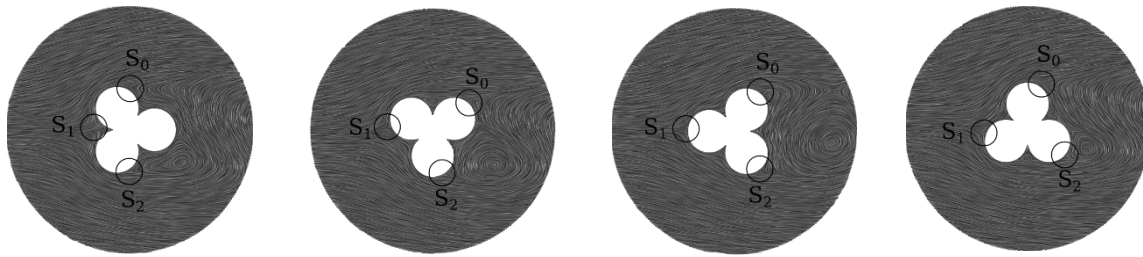
From the results of the simulation as described above, one can extract velocity and vorticity data for use in a DMD analysis. The objective is to discover coherent structures in the flow field that could help to describe some underlying mechanisms for the behaviour observed. An analogous technique to DMD is Proper Orthogonal Decomposition (POD); the distinction between the two techniques is that the former extracts the mode shapes in the temporal domain as opposed to the spatial domain in the latter (Schmid, 2010; Taira et al., 2017; Ping et al., 2021). The ability to identify mode-shapes by frequency should be useful, considering that the cases being investigated differ by rotation rate.

Consider a two-dimensional scalar or vector field $\vec{x}(x, y, t)$. A set of mode shapes $[\phi_i(x, y)]$ and corresponding eigenvalues $[\omega_i]$ are sought, so that the field can be represented by $\vec{x}(t) = \sum b_i \phi_i \exp(\omega_i t)$ where b_i is the initial mode-shape amplitude (Kutz et al., 2016). The eigenvalues determine the rate of growth or decay, and oscillation of a specific mode. Suppose that $\vec{x}(x, y, t)$ has been extracted for n timesteps then the DMD algorithm then proceeds as follows:

- Reshape $\vec{x}_j \in \mathbb{R}^{p \times q}$ into a column vector $\vec{x}'_j \in \mathbb{R}^{pq \times 1}$
- Concatenate all \vec{x}'_j for $j = 1$ to $n - 1$ into $X_{n-1} = \{\vec{x}'_1, \vec{x}'_2, \dots, \vec{x}'_{n-1}\} \in \mathbb{R}^{pq \times n}$
- Concatenate all \vec{x}'_j for $j = 2$ to n into $X_n = \{\vec{x}'_2, \vec{x}'_3, \dots, \vec{x}'_n\} \in \mathbb{R}^{pq \times n}$
- There exists a transformation A such that $AX_{n-1} = X_n$
- $A = X_n X_{n-1}^+$ where the superscript + refers to the Moore-Penrose inverse
- The eigenvectors of A correspond to the dynamic modes.

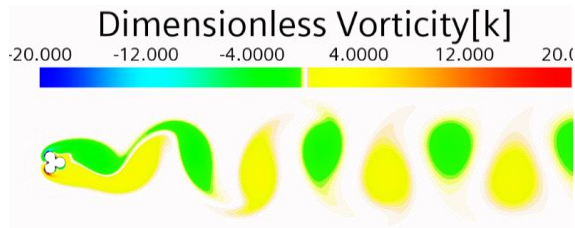
3. RESULTS AND DISCUSSION

The orientation of the cylinder cluster with respect to the free-stream changes as the cluster rotates. The effect of this changing orientation is a corresponding change in the point where the shear layer detaches and attaches from and onto the surface, respectively, and the locations of the stagnation points move. It is perhaps plausible to assume that the rotating cluster behaviour is, to an extent,

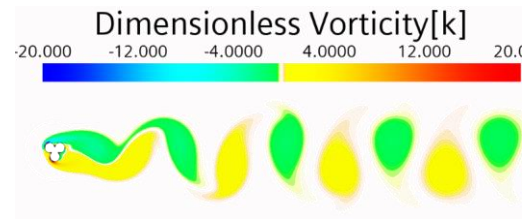


(a) Left Configuration (b) Up Configuration (c) Right Configuration (d) Down Configuration

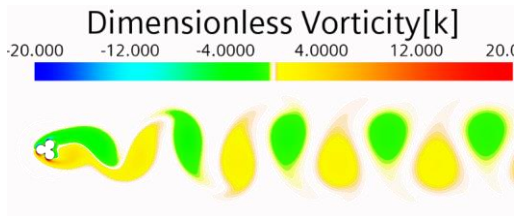
Fig. 3 Streak lines in the neighbourhood of the static three cylinder cluster for four angular displacements. The fluid is shown flowing from left to right. S_0 , S_1 , and S_2 represent the shear layer separation, stagnation, and shear layer separation points respectively



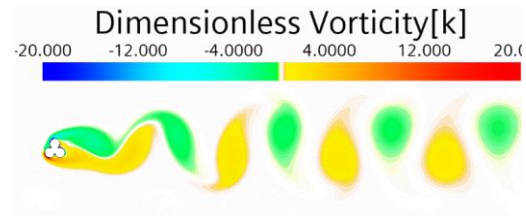
(a) Vortex shedding corresponding to the left configuration



(b) Vortex shedding corresponding to the up configuration



(c) Vortex shedding corresponding to the right configuration



(d) Vortex shedding corresponding to the down configuration

Fig. 4 Contours of the non-dimensionalised vorticity of the configurations in Fig. 3. All contours are shown at the same flow-time. In all cases, vortex shedding occurs in the 2S mode

a superposition of the behaviour of the static cluster in various orientations. The results of the stationary cylinder cluster are presented first, in § 3.1 and the discussion the results of the rotating cases presented in § 3.2. The vorticity (ζ) field is shown non-dimensionalised using free-stream velocity and the characteristic length ($\zeta U_\infty / D$).

3.1 Stationary Cylinder Cluster

Figure 3 shows the cylinder cluster in four orientations. To establish an orientation convention, consider the triangle formed by joining the centres of the cylinders in the cluster with straight lines. In the orientations in Fig. 3, one edge of this triangle will be parallel to either the x-axis or the y-axis. The orientation of the cluster is therefore according to whether the parallel edge is on the left, right, top, or bottom side of the cluster. Each orientation corresponds to a 60° anticlockwise rotation and shown at the same flow-time. These stationary cases are similar to those of (Chen et al. 2020) with $L/D = 1$ and exhibit the characteristics mentioned in that work. Each rotation shows that the locations of the separation points vary for different rotations of the cylinder cluster. The left and right configurations typify extended and reattachment flow respectively, as described by Zdravkovich (1977), while the intermediate cases (up and down) are a combination of both.

The wakes in all four orientations are shown in Fig. 4 and are unremarkable in that the wakes appear qualitatively similar and this likely invalidates the superposition assumption stated earlier. While similar, the right configuration shows that the free vortices form earlier than in the other three configurations: consider the first free vortex in the right configuration, which is still forming in the other three. Strouhal numbers for the four cases also illustrate a similar pattern; the up and down orientation have $St = 0.19$; the left orientation has $St = 0.20$; and the right orientation $St = 0.18$. These Strouhal numbers were calculated using C_L data.

The drag–lift polars are shown in Fig. 5, where we see that the up and down orientation polars are mirror reflections about the drag axis. The left and right orientations do not exhibit symmetry in the same sense as the up and down configurations; instead, they show two lobes, where each lobe is a mirror reflection of the other about the $C_L = 0$ line.

Using dynamic mode decomposition, the first four mode-shapes were extracted and are shown in Fig. 6. Each mode-shape is shown annotated by Strouhal number. The same four mode-shapes appear in all four rows ordered according to their singular values which indicate the dominance of the particular mode in the flow – singular

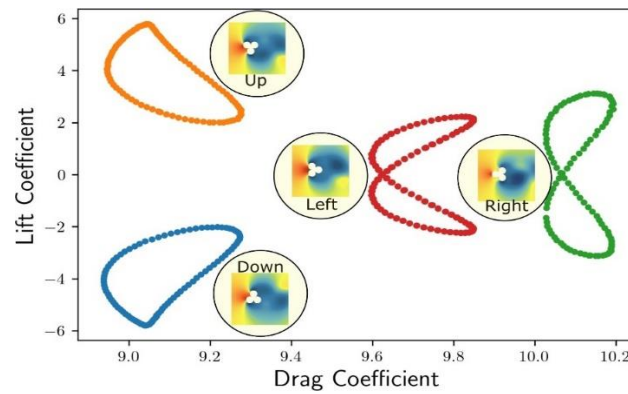


Fig. 5 Drag–Lift polars for the non-rotating three-cylinder cluster shown in Fig. 3

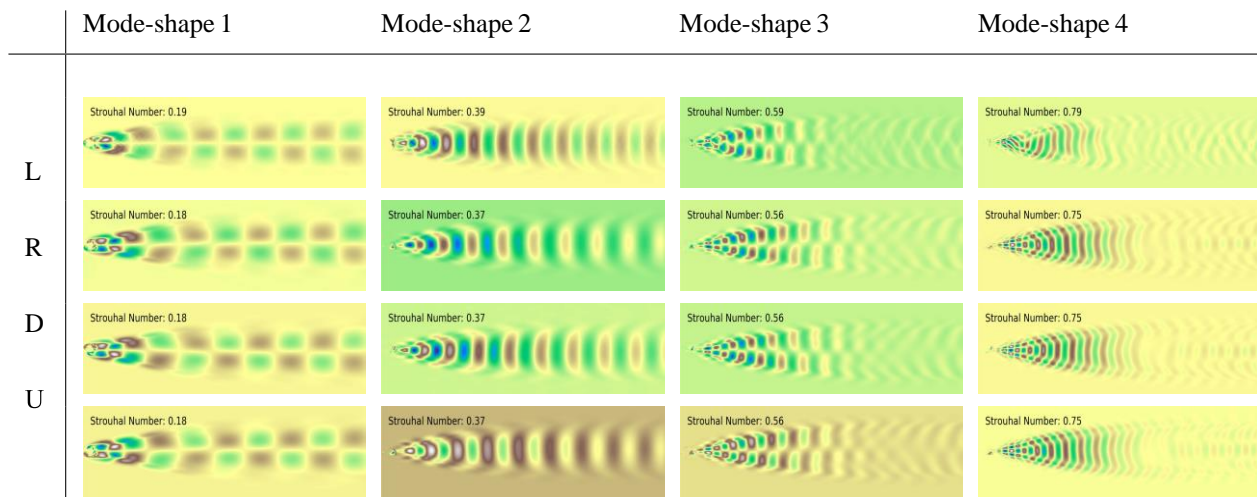


Fig. 6 First four mode-shapes derived using DMD for the left, right, up, and down configurations in the first, second, third, and fourth row respectively. These mode-shapes were calculated using the magnitude of the vorticity field, and this figure shows the complex component of each mode shape. Note that complex mode shapes come in conjugate pairs

values are determined from SVD (singular value decomposition), an intermediate step in the DMD process. Consider the Strouhal numbers: from CFD it was found that $St_{left} = 0.20$ – which corresponds to mode-shape one – while mode-shapes two and three have twice and thrice the Strouhal number from mode-shape one. A similar pattern can be observed in the right configuration. In all four configurations, mode-shapes three and four appear to be combinations of mode-shapes one and two.

When $Re > 50$, vortex shedding causes lift variation in static cylinders (Lienhard, 1966) so that the vortex shedding frequency is equal to lift oscillation frequency, and is twice the drag oscillation frequency. It can be concluded, therefore, that mode one is primarily responsible for lift oscillation and mode-shape two is responsible for drag oscillations.

3.2 Rotating Cylinder Cluster

In this section, the cylinder cluster is allowed to rotate for $0 < \Omega < 1.05$. Von Kármán vortices were observed in the wake as in the non-rotating cases, but unlike the non-rotating cases the vortices show a wide variation in pattern for different rotation rates. In the following subsection, the wake structure, drag–lift polars, and modal shapes at different rotation rates are discussed.

3.2.1 Wake Structure

The structure of the wake when $\Omega = 0.11$ is shown in Fig. 7. The wake is composed of three groups of four vortices and two counter rotating vortices on the midline, labelled G1 to 3 and S1 to 2 in Fig. 7 respectively. The G vortices occur in groups that propagate together, approximately preserving their configuration, and consist of counter-rotating components across the midline. Within G1 and G2, vortices with negative vorticity appear to coalesce downstream. Likewise, within G2 and G3, vortices with positive vorticity coalesce. Notice the directions in which the positive vorticity vortices move in group one and two (figure 7a). S1 and S2 separate vortex groups one and two from group three. All negative k-vorticity vortices and the positive k-vortex in group two tend to remain above the horizontal axis, where the positive k-vortex appears to diminish in intensity and disappear. The sigmoid shaped positive k-vortex in group three coalesces with the circular positive k-vortex below the horizontal axis.

With these observations, it is noted that vortex shedding at this rotation rate happens in several modes. Using the notation of (Matharu et al., 2021) and referring to Fig. 8c, we see that each group starts from a PS+S mode and evolves into S modes in various degrees of

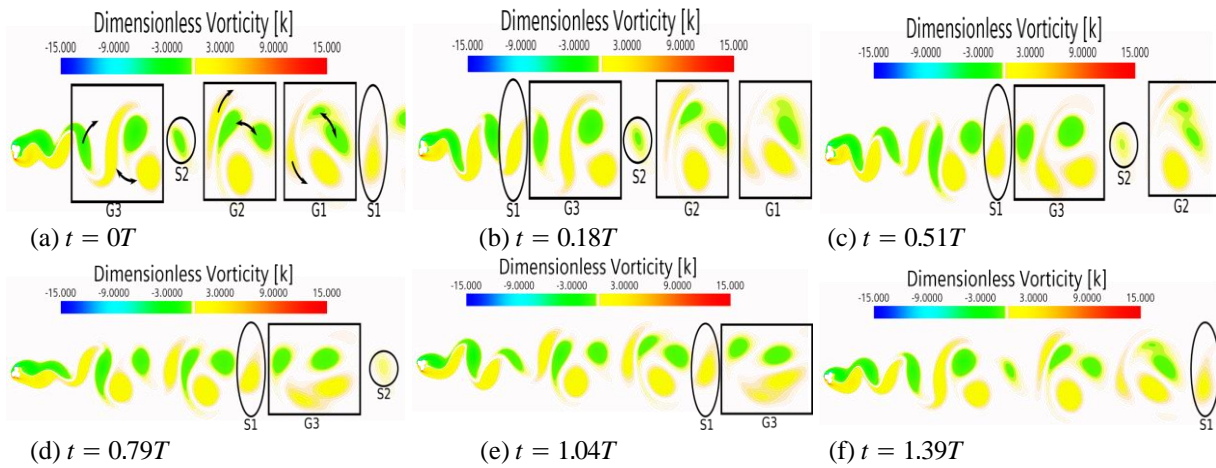


Fig. 7 Flow around a rotating cylinder cluster with $\Omega = 0.11$. T is the period of rotation. Vortices have been grouped into three groups, G1, G2, and G3. Effectively isolated vortices have been labelled S1 and S2

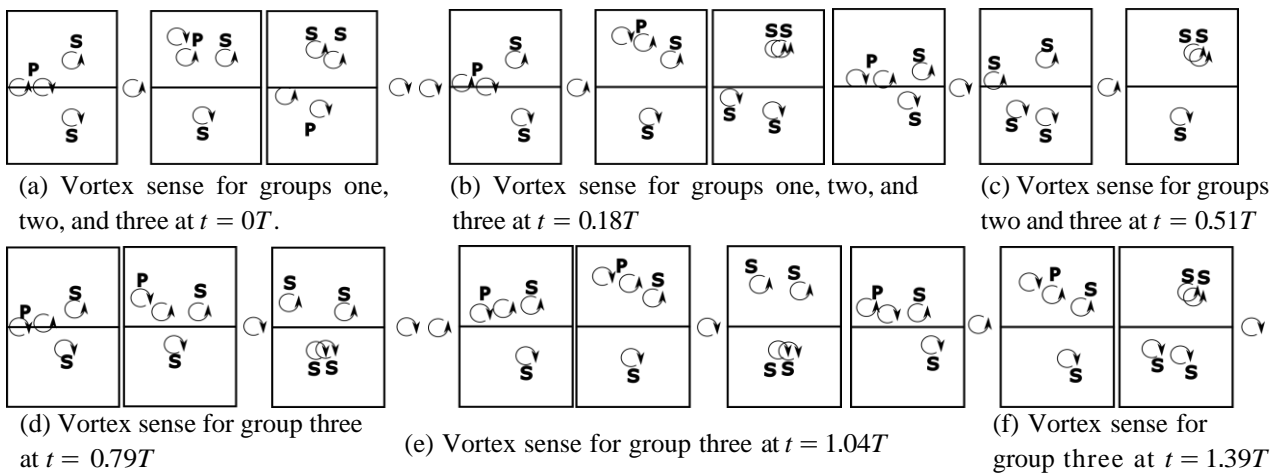


Fig. 8 Vortex sense for $\Omega = 0.11$ corresponding to Figure 7 where T is the period of rotation. Each subfigure here corresponds to a subfigure in Fig. 7

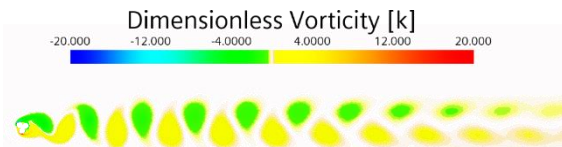


Fig. 9 Well-behaved vortex street at $\Omega = 0.22$

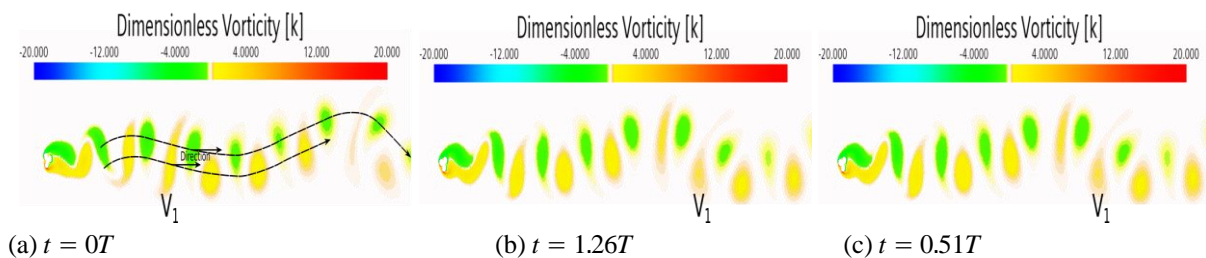


Fig. 10 Flow around a rotating cylinder cluster with $\Omega = 0.33$. T is the time taken to complete one rotation of the cylinder cluster

coalescence. Group one evolves into S+2S mode where the vortices above the axis have completely merged; group two, evolves into a 2S+S mode with the vortex below the axis maintaining its solitude throughout this observation window; and group three ends up in a 2S+2S mode with the vortices below the axis in a final stage of merging. This dynamic behaviour likely continues beyond this observation window.

The wake when the rotation rate is doubled ($\Omega = 0.22$) is shown in Fig. 9. At this rotation rate, the cluster sheds vortices in the 2S mode. When $\Omega = 0.33$, a Von Kármán vortex street is formed as before, except that the entire vortex street oscillates about the horizontal axis (Fig. 10a). Each shed vortex propagates parallel to the horizontal axis, but subsequent vortices are shed at different vertical

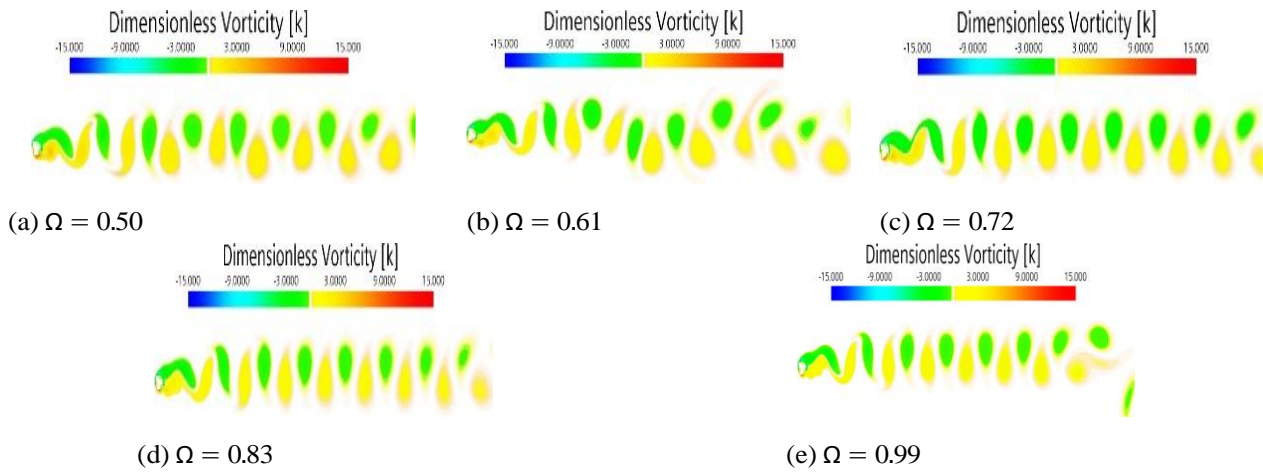


Fig. 11 Flow around a rotating cylinder cluster for $\Omega > 0.49$

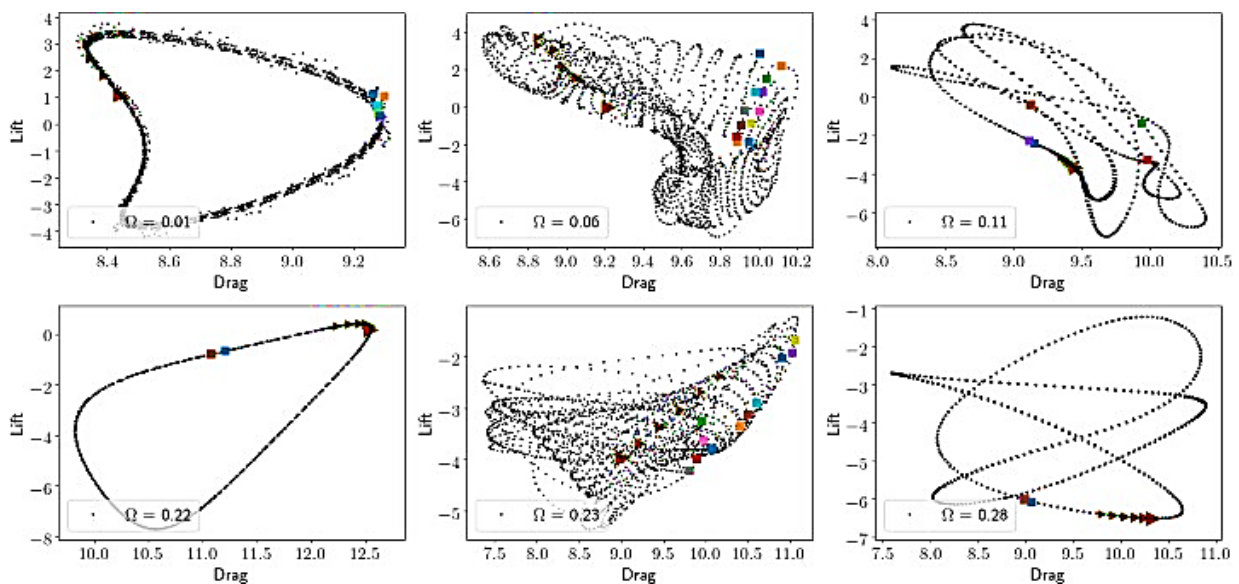


Fig. 12 Lift–Drag polars for $\Omega < 0.3$. $\Omega = 0.011$, $\Omega = 0.22$, and $\Omega = 0.28$ appear to form closed orbits while $\Omega = 0.06$ and $\Omega = 0.23$ seem to be space filling. Eleven square symbols were plotted showing lift and drag after a 360° rotation of the cylinder cluster, with the triangles showing the direction of polar variation with rotation (read from small to large triangle)

distances from the axis, resulting in a low frequency oscillation.

For $\Omega > 0.44$ the wake adopts a more consistent structure as illustrated in Fig. 11 except Fig. 11b which shows the wake oscillation observed in Fig. 10, the wake at other rotation rates has a consistent 2S vortex shedding mode characterised by counter rotating vortices symmetric about the horizontal axis.

Thus, the case for vortex shedding around a rotating cylinder cluster can be categorised into three stages: a complex first stage ($0 < \Omega < 0.3$), a simple second stage with secondary vortex street oscillation ($0.3 < \Omega < 0.6$), and a third stage with a typical Von Kármán vortex street ($\Omega > 0.6$).

3.3 Lift–Drag Polars

The lift–drag polars for rotating cylinder clusters show more complex patterns than those observed for static cylinders in Fig. 5 and can be categorised similarly to the

vortex shedding patterns where polars for $\Omega < 0.3$, $0.3 < \Omega < 0.6$, and $0.6 < \Omega < 1$ have similar characteristics. In Fig. 5 it was seen that the left and right oriented clusters have lift–drag polars with two loops – due to the Strouhal number based on drag (St_D) being twice that based on lift (St_L) – while the up and down orientations have a single loop (lift and drag based Strouhal numbers are equal). This is typical of Lissajous figures and circular harmony curves, (Pook, 2011; Figueroa et al., 2017) where St is a proxy for shedding frequency. The complexity of the lift–drag polars thus depends on the ratio, St_D/St_L which in this case is not always an integer and may be irrational. Therefore, we expect that when St_D/St_L is rational and irrational, the lift–drag polars will form closed and open orbits respectively. The former case results in the curve filling up the domain as time progresses (Figueroa et al., 2017). St_D/St_L is irrational when either St_D and St_L is irrational.

Lift–drag polars for selected cases where $\Omega < 0.3$ are shown in Fig. 12. A closed curve is formed when

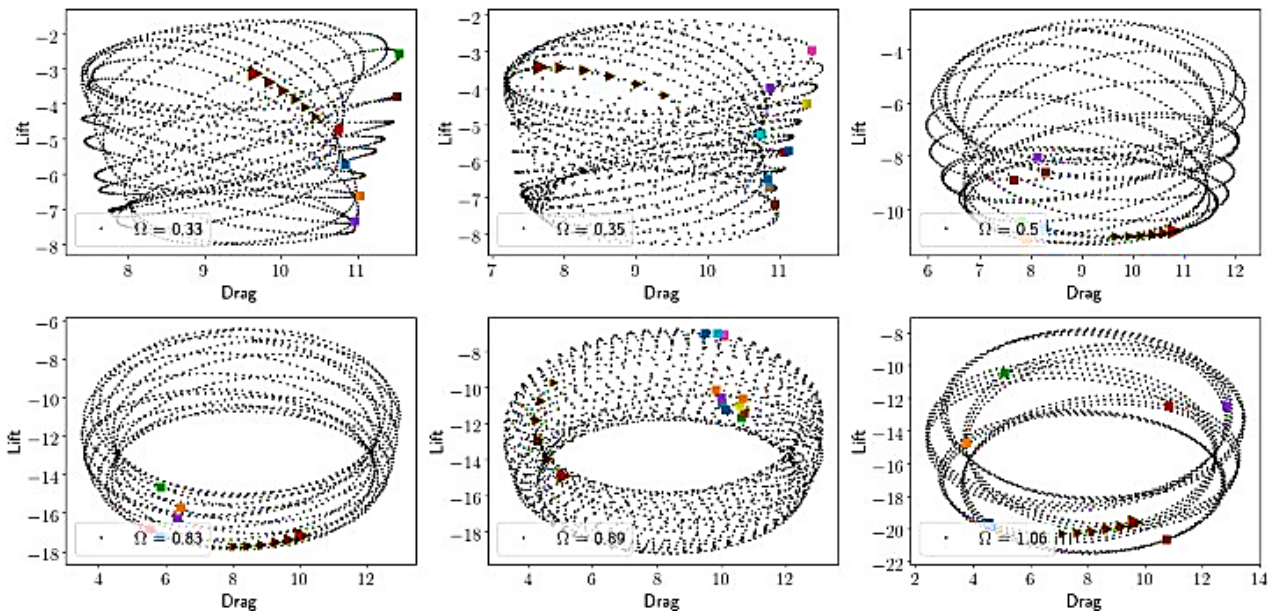


Fig. 13 Lift–Drag polars for $\Omega > 0.3$. All curves are space filling. The squares show positions after a full rotation of the cylinder cluster, and the triangles show direction

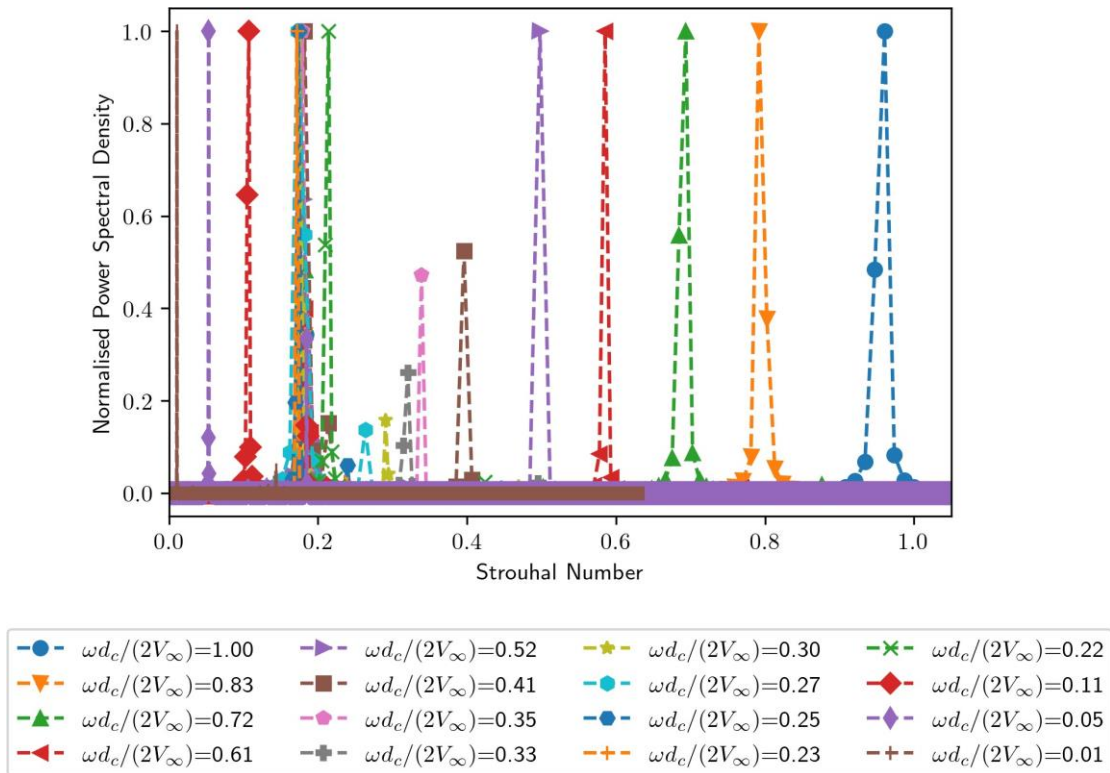


Fig. 14 Normalised power spectral density (PSD) for Strouhal numbers at several non-dimensionalised rotation rates

$\Omega = 0.22$; increasing Ω to 0.23 results in a disconnected space filling as shown in the figure, implying strong sensitivity to rotation rate. Whether a curve is closed or not is a function of Strouhal number and rotation rate, Ω . Where the curves are connected or almost connected, the cluster completes each rotation consistently at the same lift and drag values ($\Omega \in \{0.01, 0.22, 0.28\}$).

In contrast, for $\Omega = 0.11$ the starting positions are in four clusters. Recall that at this rotation rate, the shed vortices also occurred in groups; three distinct vortex

clusters and two single vortices. Could there be a relation between the cluster of starting positions and the vortex shedding groups? Where the polars are clearly disconnected, the starting positions are scattered along the polars ($\Omega \in \{0.06, 0.23\}$). Select lift–drag polars between $\Omega = 0.3$ and $\Omega = 0.6$ are shown in Fig. 13 in the first row, while the second row shows $\Omega > 0.6$. The polars clearly have common characteristics as described above and are more consistent in terms of structure. With consistency comes stability; changing Ω from 0.33 to 0.35

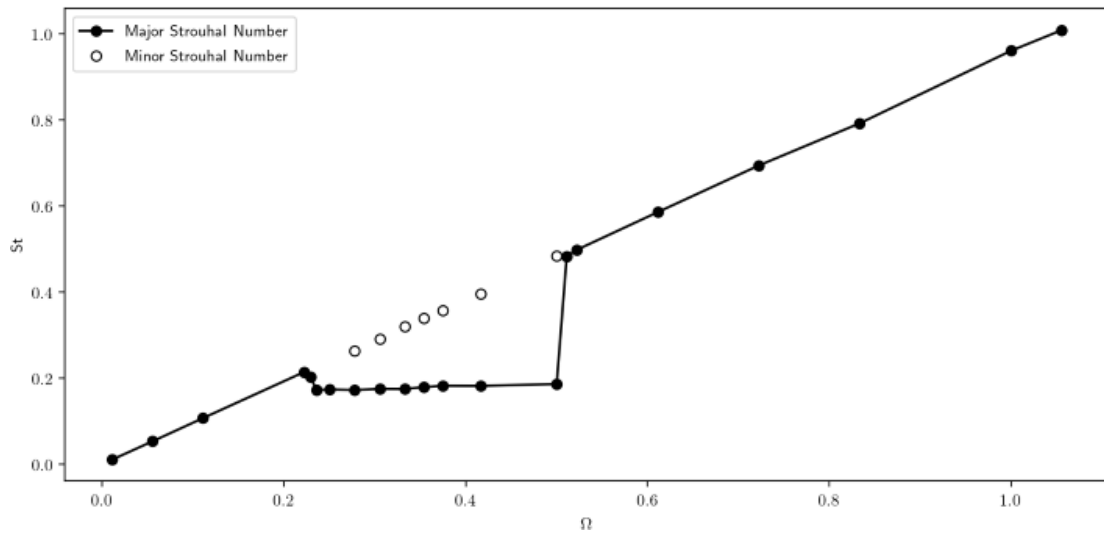


Fig. 15 Strouhal numbers for $0 < \Omega < 1$. Strouhal numbers were categorised between major and minor based on power spectral distribution as seen in Fig. 14. The larger and smaller PSD correspond to major and minor St respectively

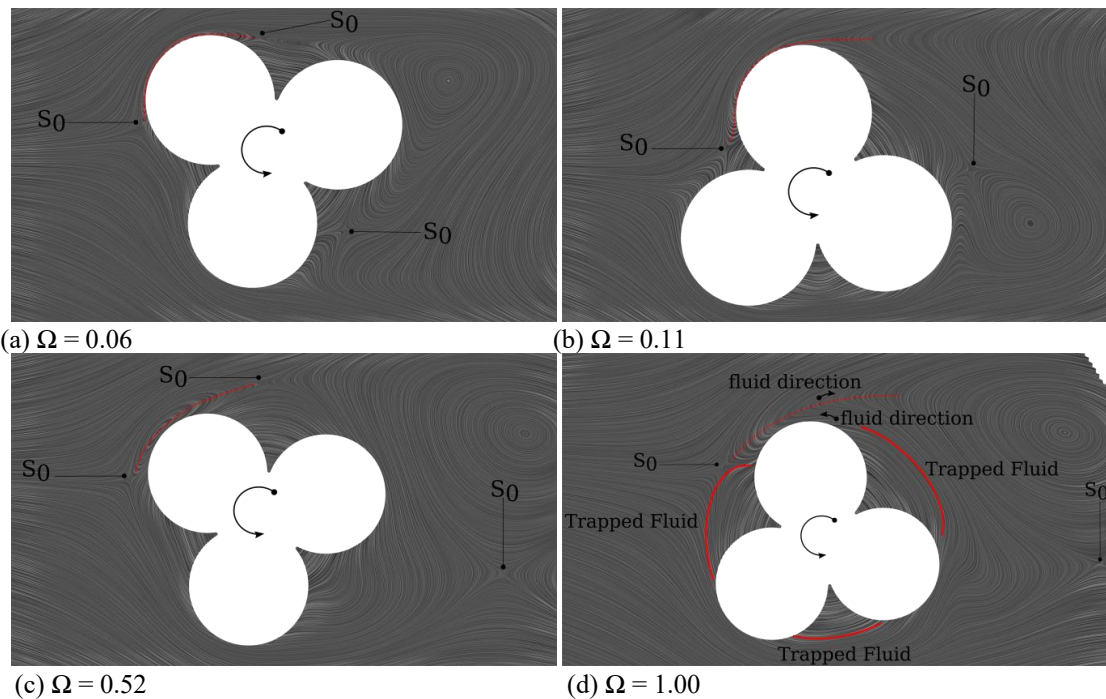


Fig. 16 Flow in the neighbourhood of the cylinder cluster, constructed using a line integral convolution of the velocity vector field. S_0 marks the stagnation points in the flow field. The curved line on the cylinder above the horizontal is an estimate of the boundary-layer

does not result in as drastic a change in the polar plot as was the case for Ω less than 0.3.

The classification of wake and lift–drag polars in terms of Ω given above is supported by Fig. 15 which shows variation of St with rotation rate. The curve shows that the variation is linear, interrupted by a transition with two Strouhal numbers (a minor and a major Strouhal number). The minor Strouhal number continues the linear trend, while the major Strouhal number forms a flat valley at a constant Strouhal number. This region acts as a transition between the two distinct regions; the first region marked by varied vortex shedding patterns and the second simpler region. Major and minor Strouhal numbers are categorised according to their power spectrum densities

(PSD) where the PSD for the major Strouhal number is greater than that of the minor Strouhal number (Fig. 14), i.e., all peaks with PSD = 1 were categorised as major and the rest as minor. Notice how, as will be seen again in Fig. 15, all the minor Strouhal number lie between 0.2 and 0.5.

To understand the origins of these distinct regions, consider a detailed view of the flow around the cluster (Fig. 16). Due to the no slip boundary condition, the fluid in contact with the cluster of cylinders has non-dimensionalised velocity Ω . With the cluster rotating anti-clockwise, cylinders above and below the horizontal are counter and co-directional to the free-stream strongly influencing the boundary layer, shear-layer-separation-point, and stagnation points. Unlike the case of a single

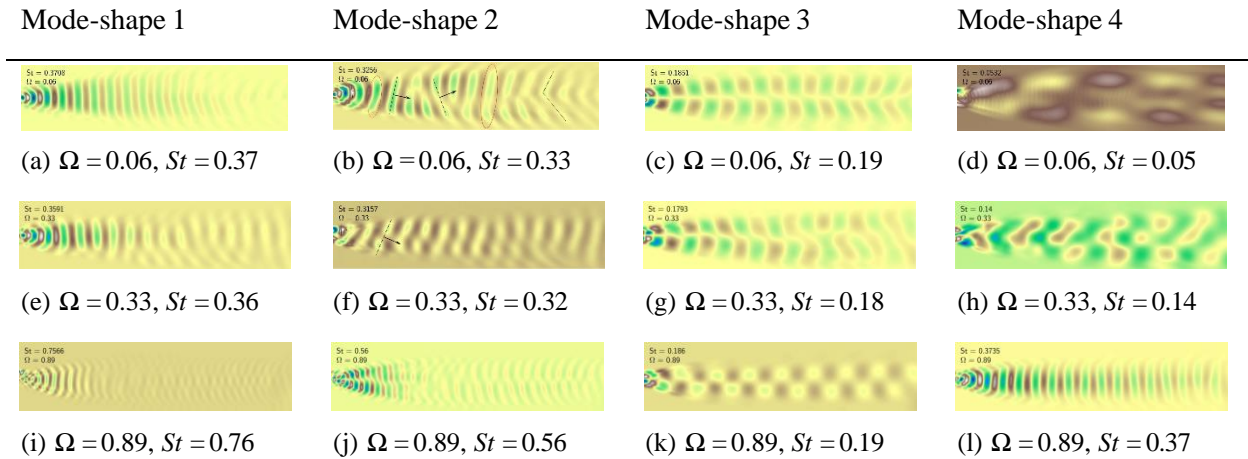


Fig. 17 First four mode-shapes calculated using the magnitude of the vorticity field at the respective non-dimensionalised rotation rates. The mode-shapes for each rotation rate are arranged according to decreasing singular values. The figure shows the complex component of the mode-shape, therefore, each mode-shape shown here has a corresponding conjugate

cylinder where there is a one stagnation point which settles on one side of a rotating cylinder (Sierra et al., 2020), the cluster has multiple stagnation points which merge, form, and move along with the rotating cluster. Some stagnation points are shown in Fig. 16. The boundary-layer thickness when a cylinder is above the horizontal tends to increase with increases in rotation rate. Figure 16b and 16d illustrate this well. Also, consider the fluid trapped between two adjacent cylinders: as Ω increases from 0.06 to 1.00, the region of trapped fluid increases until it and the cluster form a virtual single cylinder from the perspective of the free-stream. Therefore, the trend observed in Fig. 15, excluding $0.3 < \Omega < 0.6$, corresponds to vortex shedding around an effectively bare cylinder cluster (bare because the trapped region is small) and a covered cluster (the trapped region is large) for $\Omega < 0.3$ and $\Omega > 0.6$ respectively. The intermediate region corresponds to the transition between the two states. It may, perhaps, also be interesting to consider what influence rotation has on Moffatt eddies (Moffatt, 2021) that form between adjacent cylinders.

3.4 Modes from DMD

Figure 17 shows the mode-shapes as calculated using DMD for three rotation rates ($\Omega \in \{0.06, 0.33, 0.89\}$). The three rotation rates were chosen to represent the three regimes identified in the section above. Mode-shapes for the rotating cluster are qualitatively similar to those of the static clusters and similar mode-shapes appear to have equal Strouhal numbers; for instance, compare mode-shapes 1, 1, and 4 for $\Omega = 0.06, 0.33,$ and 0.89 respectively, with similar mode-shapes in Fig. 6 where $St \approx 0.37$. As before, mode-shapes 1, 1, and 4 for the successive rotation rates are characterised by longitudinal oscillations and hence have a strong effect on C_D variation. Mode-shape 3 in all rotation rates is similar to mode-shapes 1, 2, 1, and 1 for the cases in Fig. 6 and are each associated with transverse oscillations implying a strong effect on C_L . Notice that the Strouhal number associated with the longitudinal mode-shape is twice that associated with the transverse mode-shape for all rotation rates,

which would imply connected lift–drag polars. Mode-shape 2 for the first two rotations appears to be a modification of the longitudinal mode-shape with a break in symmetry; an initially contiguous valley splits into two downstream. When $\Omega = 0.33$, a similar split in an initially contiguous valley is observed. Possibly, this is the influence of rotation on the longitudinal mode-shape. Similarly, the transverse mode-shapes for the first two rotation rates, mode-shape 4 is a modification of mode-shape 3. The ratios of Strouhal numbers associated with these modifier mode-shapes do not appear to be rational as was the case for the transverse and longitudinal mode-shapes, so that they are the possible sources for the disconnection in the drag–lift polars observed in Fig. 12.

Now, consider the mode-shapes associated with $\Omega = 0.89$; clearly they are similar to the mode-shapes in static cases (Fig. 6) except for the order in which the mode-shapes appear. Despite the similarity in mode-shapes, the corresponding drag–lift phase plot is space filling. It has already been noted that the longitudinal and transverse mode Strouhal numbers have a ratio of two so that the cause for the disconnection in the phase plot must be caused by the modifier mode-shapes (1 and 2); the Strouhal number ratio of these two mode-shapes does not appear to be rational.

4. CONCLUSIONS

This study sought to investigate the influence of rotation on a rotating cluster of cylinders for $Re = 100$ and non-dimensionalised rotation rates (Ω) between zero and one. For this case, it was noted that:

- For non-dimensionalised rotation rates (Ω) between zero and one, the flow field can be categorised into three regimes: the first regime when Ω is less than 0.3; a transitional regime between 0.3 and 0.5; and a third regime above 0.5. These boundaries were estimated from simulations performed at discrete points.

- The first regime C_D – C_L phase portraits are sensitive to Ω . For some Ω , the loci are closed while for most cases, the loci are disconnected and possibly space-filling.
- The first regime exhibits more complex vortex shedding patterns which, similarly to the phase portraits are sensitive to Ω .
- As Ω increases beyond 0.5, the vortex street behaviour becomes simpler, but a secondary low frequency oscillation can also be seen.
- The major mode-shapes extracted from the vorticity field each influence either drag or lift. This is based on the observation that mode-shape frequency was seen to correspond to either lift or drag oscillation frequencies.
- For the non-rotating cases, the minor mode-shapes are harmonics of the major-mode shapes; however, the rotating cases do not show a similar relationship, instead the ratio of Strouhal numbers between minor and major mode-shapes seem to be irrational.

Two obvious extensions to this study would be to investigate other Reynolds numbers and clusters.

CONFLICT OF INTEREST

The authors have no conflicts of interest to disclose.

AUTHORS CONTRIBUTION

B. B. Ndebele carried out all aspects of this work, including conceptualisation. I. M. A. Gledhill contributed to conceptualisation, methodology, and editing.

REFERENCES

- Bai, X., Ji, C., Grant, P., Phillips, N., Oza, U., Avital, E. J., & Williams J. J. R. (2021). Turbulent flow simulation of a single-blade magnus rotor. *Advances in Aerodynamics*, 3. <https://doi.org/10.1186/s42774-021-00068-9>
- Carmo, B. S., Sherwin, S. J., Bearman, P. W., & Willden, R. H. J. (2008). Wake transition in the flow around two circular cylinders in staggered arrangements. *Journal of Fluid Mechanics*, 597, 1–29. <https://doi.org/10.1017/S0022112007009639>
- Chen, W., Ji, C., Alam, M. M., Williams, J., & Xu, D. (2020). Numerical simulations of flow past three circular cylinders in equilateral-triangular arrangements. *Journal of Fluid Mechanics*, 891, A14. <https://doi.org/10.1017/jfm.2020.124>
- Figuroa, A., Cuevas, S., & Ramos, E. (2017). Lissajous trajectories in electromagnetically driven vortices. *Journal of Fluid Mechanics*, 815, 415–434. <https://doi.org/10.1017/jfm.2017.55>
- Inoue, T., Rheem, C. K., Kyo, M., Sakaguchi, H., & Matsuo, M. Y. (2013). *Experimental study on the characteristics of VIV and whirl motion of rotating drill pipe*. ASME 2013 32nd International Conference on Ocean, Offshore and Arctic Engineering. <https://doi.org/10.1115/OMAE2013-10182>
- Kutz, J. N., Brunton, S. L., Brunton, B. W., & Proctor, J. L. (2016). *Dynamic mode decomposition*. Society for Industrial and Applied Mathematics. <https://doi.org/10.1137/1.9781611974508>
- Lienhard, J. N. (1966). *Synopsis of lift, drag, and vortex frequency data for rigid circular cylinders* (Vol. 300). Pullman, WA: Technical Extension Service, Washington State University. Retrieved May 11, 2023, from <https://www.uh.edu/engines/vortexcylinders.pdf>
- Matharu, P. S., Hazel, A. L., & Heil M. (2021). Spatio-temporal symmetry breaking in the flow past an oscillating cylinder. *Journal of Fluid Mechanics*, 918, A42. <https://doi.org/10.1017/jfm.2021.358>
- Mittal, S., & Kumar, B. (2003). Flow past a rotating cylinder. *Journal of Fluid Mechanics*, 476, 303–334. <https://doi.org/10.1017/S0022112002002938>
- Moffatt, H. (2021). Some topological aspects of fluid dynamics. *Journal of Fluid Mechanics*, 914, P1. <https://doi.org/10.1017/jfm.2020.230>
- Phillips, T. S., & Roy, C. J. (2014). Richardson extrapolation-based discretization uncertainty estimation for computational fluid dynamics. *Journal of Fluids Engineering*, 136. <https://doi.org/10.1115/1.4027353>
- Ping, H., Zhu, H., Zhang, K., Zhou, D., Bao, Y., Xu, Y., & Han, Z. (2021). Dynamic mode decomposition based analysis of flow past a transversely oscillating cylinder. *Physics of Fluids*, 33, 033604. <https://doi.org/10.1063/5.0042391>
- Pook, L. P. (2011). *Understanding pendulums: A brief introduction*. Springer Netherlands. <https://doi.org/10.1007/978-94-007-1415-1>
- Roache, P. J. (1994). Perspective: A method for uniform reporting of grid refinement studies. *Fluids Engineering*, 116, 405–413. <https://doi.org/10.1115/1.2910291>
- Roshko, A. (1954). *On the development of turbulent wakes from vortex streets*. California Institute of Technology. Retrieved May 25, 2023, from <https://ntrs.nasa.gov/citations/19930092207>
- Schmid, P. J. (2010, 8). Dynamic mode decomposition of numerical and experimental data. *Journal of Fluid Mechanics*, 656, 5–28. <https://doi.org/10.1017/S0022112010001217>
- Schulmeister, J. C., Dahl, J. M., Weymouth, G. D., & Triantafyllou, M. S. (2017). Flow control with rotating cylinders. *Journal of Fluid Mechanics*, 825, 743–763. <https://doi.org/10.1017/jfm.2017.395>
- Sierra, J., Fabre, D., Citro, V., & Giannetti, F. (2020). Bifurcation scenario in the two-dimensional laminar flow past a rotating cylinder. *Journal of Fluid*

- Mechanics*, 905, A2.
<https://doi.org/10.1017/jfm.2020.692>
- Sumner, D., Price, S. J., & Paidoussis, M. P. (2000). Flow-pattern identification for two staggered circular cylinders in cross-flow. *Journal of Fluid Mechanics*, 411, 263–303.
<https://doi.org/10.1017/S0022112099008137>
- Taira, K., Brunton, S. L., Dawson, S. T. M., Rowley, C. W., Colonius, T., McKeon, B. J., Schmidt, O. T., Gordeyev, S., Theofilis, V., & Ukeiley, L. S. (2017). Modal analysis of fluid flows: An overview. *AIAA Journal*, 55, 4013–4041.
<https://doi.org/10.2514/1.J056060>
- Taira, K., Hemati, M. S., Brunton, S. L., Sun, Y., Duraisamy, K., Bagheri, S., Dawson, S. T. M., & Yeh, C. A. (2020). Modal analysis of fluid flows: Applications and outlook. *AIAA Journal*, 58, 998–1022.
<https://arc.aiaa.org/doi/10.2514/1.J058462>
- Wang, H., Yan, Y. H., Chen, C. M., Ji, C. N., & Zhai, Q. (1996). Numerical investigation on vortex-induced rotations of a triangular cylinder using an immersed boundary method. *China Ocean Engineering*, 33, 723–733.
<https://doi.org/10.1007/s13344-019-0070-0>
- Williamson, C. H. K., & Roshko A. (1988). Vortex formation in the wake of an oscillating cylinder. *Journal of Fluids and Structures*, 2, 355–381.
[https://doi.org/10.1016/S0889-9746\(88\)90058-8](https://doi.org/10.1016/S0889-9746(88)90058-8)
- Zdravkovich, M. M. (1977). Review—review of flow interference between two circular cylinders in various arrangements. *Journal of Fluids Engineering*, 99, 618–633.
<https://doi.org/10.12691/ajme-5-3-3>